Editors' Suggestion

$L1_0$ rare-earth-free permanent magnets: The effects of twinning versus dislocations in Mn-Al magnets

Yuxiao Jia,[1] Yuye Wu,[1,2,*] Shuang Zhao,[1] Shulan Zuo,[1] Konstantin P. Skokov,[2] Oliver Gutfleisch,[2] Chengbao Jiang,[1,†] and Huibin Xu[1]

[1]*Key Laboratory of Aerospace Materials and Performance (Ministry of Education), School of Materials Science and Engineering, Beihang University, Beijing 100191, People's Republic of China*

[2]*Institute of Materials Science, Technical University of Darmstadt, Darmstadt 64287, Germany*

(Received 25 June 2020; accepted 13 August 2020; published 10 September 2020)

Defects of various kinds strongly affect local magnetic anisotropy and thus play a crucial role in coercivity in high-performance permanent magnets. In particular, in rare-earth-free permanent magnetic alloys with $L1_0$ structure microstructural defects deserve special attention. In this work, we report on the "negative" effect of twin structure, and the "positive" effect of dislocations on the coercivity is clarified in a systematic experimental study of $L1_0$-MnAl alloys. We find that the nucleation of magnetization reversal is preferentially activated along the twin boundaries and grows into the twin stripes. This suggests that twin structure reduces the domain wall nucleation field, so that the coercivity decreases by approximately 50% according to the direct comparison of twin-free and twinned magnets. In contrast, dislocations dramatically enhance the coercivity by acting as the pinning center, and a high density of dislocations can modify the dominant coercivity mechanism from nucleation to pinning in severely deformed MnAl magnets. With a decreasing dislocation density, the pinning field remains as a constant while the coercivity reduces monotonously, indicative of the "strong pinning" effect of dislocations on the magnetic domain wall, generating a positive correlation between coercivity and density of dislocation. High coercivity from 424 to 328 kA/m is obtained in deformed and annealed magnets with different densities of dislocations. Thus, the combination of eliminating twin structure and introducing high-density dislocations could overcome the present bottleneck in magnetic performance. This work may inspire avenues for the development of $L1_0$ rare-earth-free permanent magnetic alloys, and set up a pathway for accelerating the application process.

DOI: 10.1103/PhysRevMaterials.4.094402

I. INTRODUCTION

Permanent magnetic materials are already and will be under increasing demand in many high-tech applications, especially as they enable highly efficient advanced energy conversion and energy recovery devices [1]. The replacement of fossil-fuel-based transportation by electric motors based on high-performance permanent magnets is one of the main drivers in the market [2,3]. Magnets allow one to minimize the weight and volume of devices and to realize highly efficient wind power generation and plug-in hybrid vehicles, etc. [2–4]. Rare-earth-based permanent magnets (mostly Nd-Fe-B) and ferrite permanent magnets dominate the global market, occupying approximately 90% of the share in terms of market value [2,5]. The rare-earth-based Nd-Fe-B permanent magnets [with $(BH)_{\max}$ of $350-440\,\mathrm{kJ/m^3}$ and theoretical $(BH)_{\max}^{\mathrm{theo}} = 512\,\mathrm{kJ/m^3}$] often require substantial usage of heavy rare-earth elements (Dy and Tb) or strategic element Co, resulting in ultrahigh costs [2]. The ferrite permanent magnets on the other hand have relatively low magnetic properties by theoretical analysis [$(BH)_{\max}^{\mathrm{theo}} = 45\,\mathrm{kJ/m^3}$] and experiments [$(BH)_{\max}^{\mathrm{exp}} < 34\,\mathrm{kJ/m^3}$] [1,6]. Therefore, alternative candidate systems of relatively low cost and high performance are needed to plug the gap between rare-earth-based permanent magnets and ferrites [1,5]. The obtaining of high performance of rare-earth-free magnets is a difficult but not impossible task, and the feasibility of it has also been proved [4].

Several rare-earth-free permanent magnetic candidate systems with $L1_0$ crystal structure have been studied, including MnAl, MnGa, FeNi, FePt, FePd, FeCo, etc. All of them show attractive intrinsic properties, as summarized in Table S1 in the Supplemental Material [7]; also see [8–15], but the understanding of the coercivity mechanisms responsible for their hard magnetic properties is still unsatisfactory or even the basic knowledge to induce coercivity at all is hardly existent. Based on the previous studies, ideal nano- or microstructure should be possessed for obtaining acceptable extrinsic characteristics [16]. However, the influence of specific features of microstructure on coercivity is highly ambiguous. For instance, the twin structure is a common microstructural feature in $L1_0$ alloys [8,17,18], and is formed during the solid-state transformation from the high-temperature face-centered-cubic or closely compacted hexagonal phase with high symmetry to the ferromagnetic $L1_0$ phase with low symmetry [8,18–20]. The typical morphologies of twin structures in $L1_0$-MnAl including nanotwins and macrotwins are shown in Fig. 1,

*wuyuye@buaa.edu.cn
†jiangcb@buaa.edu.cn

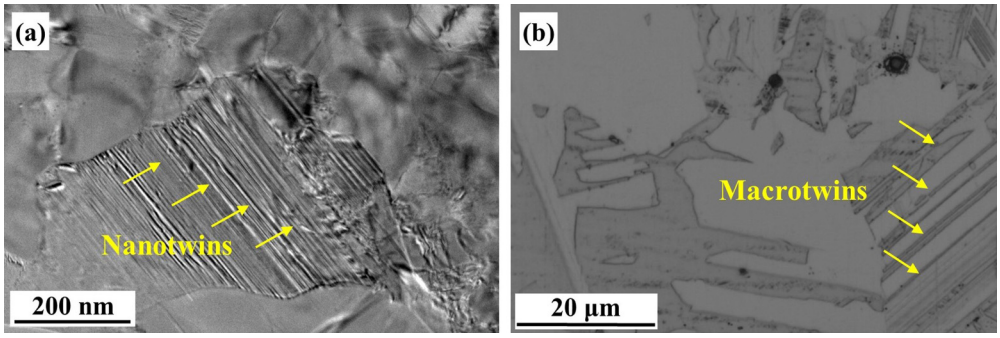

FIG. 1. (a) TEM image showing the nanotwin structure in $L1_0$-MnAl alloy. (b) Optical morphologies showing the macrotwin structure in $L1_0$-MnAl alloy.

and previous works also reported the twin structure in other $L1_0$ alloys [8,18,21,22]. In MnAl, the high-temperature parent phase has several equivalent shearing directions so the isotropic self-accommodated twin structure is always formed after transformation of parent phase to ferromagnetic $L1_0$ phase [19]. In FePt, FePd, and CoPt alloys, the lattice misfit between the cubic and tetragonal phase induces the formation of twin structure leading to minimizing the strain energy [23].

Since the 1970s, the effect of twin structure on magnetic properties has been investigated, but it still remains controversial. Jakubovics *et al.* [24] and Landuyt *et al.* [25] proposed that the twin boundaries act as a pinning center for domain wall movement in MnAl permanent magnet materials, contributing to the coercivity. Klemmer *et al.* [8] and Vlasova *et al.* [22] reported that high density of twin structure was likely to degrade the coercivity in $L1_0$ FePd, CoPt, and FePt alloys. Tanaka *et al.* [19] related magnetic softening to the polytwin structure formed in $L1_0$-FePt alloys, rejecting the pinning effect of twin structure. Recently, Bance *et al.* [26] showed, using micromagnetic simulations, that twin structure will deteriorate coercivity, squareness, and energy product.

However, despite the vast literature on this topic, due to the absence of the effective method of regulating the twin structure in these $L1_0$ alloys, it is very difficult to directly compare the performance between twin-free and twinned alloys, realizing the role of twin in magnetic properties. Besides the twin structure, the confirmation of "positive" or "negative" effects of other microstructural features on coercivity are also required, so that positive microstructure could be introduced into the $L1_0$ systems in order to further enhance the coercivity. The understanding of the function of the defects is of crucial importance in promoting the application of the $L1_0$ rare-earth-free permanent magnets.

In this work, we focus on Mn-Al permanent magnetic alloys because their cost is much lower than FePt, CoPt, FePd, and MnGa, etc., and the $L1_0$ phase is relatively easier to obtain compared with MnGa and FeNi alloys [5]. The investigations on Mn-Al alloying show that doping of transition alloys generally decreases the stability and intrinsic magnetic property, while a carbon atom will stabilize the $L1_0$ phase and introduce a tiny effect on properties [27,28]. In this work, the composition of $(Mn_{0.54}Al_{0.46})_{97}C_3$ is chosen for a comprehensive study, because the solubility of carbon in Mn-Al is approximately 3%, and the alloy with this composition has been reported by Zhao *et al.* [27] to have optimal thermal stability. We illuminated the function of microstructural features including twin structure and dislocations in coercivity and the corresponding hardening mechanism. The comparison in magnetic properties between twinned and twin-free magnets and interaction between twin boundaries and domain wall motion process indicate the effect of twin structure on the coercivity mechanism. Furthermore, the dislocations were proved to enhance the coercivity significantly by acting as pinning centers and modifying the coercivity mechanism from nucleation dominated to pinning dominated. This work may promote the understanding between microstructure defects and performance in $L1_0$ rare-earth-free permanent magnets, and open avenues to overcome the current bottleneck in the magnetic performance of rare-earth-free magnets.

II. EXPERIMENT

The original $(Mn_{0.54}Al_{0.46})_{97}C_3$ ingots were prepared in a nonconsumable arc melting furnace under Ar atmosphere. The ingots were melted and then cast into a copper mold to obtain rods with the diameter of 7 mm. The preparation methods of an $A3$ phase single crystal, the twin-free, and twinned bulk samples were described previously in detail in Ref. [29]. Both the twin-free and twinned bulk $(Mn_{0.54}Al_{0.46})_{97}C_3$ samples were gently ground in an agate mortar by using an agate pestle. Subsequently, the particles were mixed with epoxy and aligned under a magnetic field of 1.6 MA/m to fabricate the oriented bonded magnets. The severely deformed samples were prepared by the high-pressure torsion (HPT) method under a pressure of 5 GPa. The schematic diagrams of the HPT method and the microstructure before and after deformation, as well as the picture of the deformed samples, are shown in Fig. S1 of the Supplemental Material [7]. The microstructures were observed by a LEICA DM4000 optical microscope, and a JEOL 2100F and F20 field emission transmission electron microscope (TEM). The phase analysis and orientation confirmation were performed by D/max 2500 x-ray diffraction (XRD) with Cu $K\alpha$ radiation ($\lambda = 0.154$ nm). The crystal texture and defects density are investigated through electron backscattered diffraction (EBSD) measurement of a Zeiss Sigma 300 field emission scanning electron microscope (SEM). The magnetic properties were measured in a physical property measurement system (PPMS), under the maximum magnetic field of 4.8 MA/m at 300 K. The

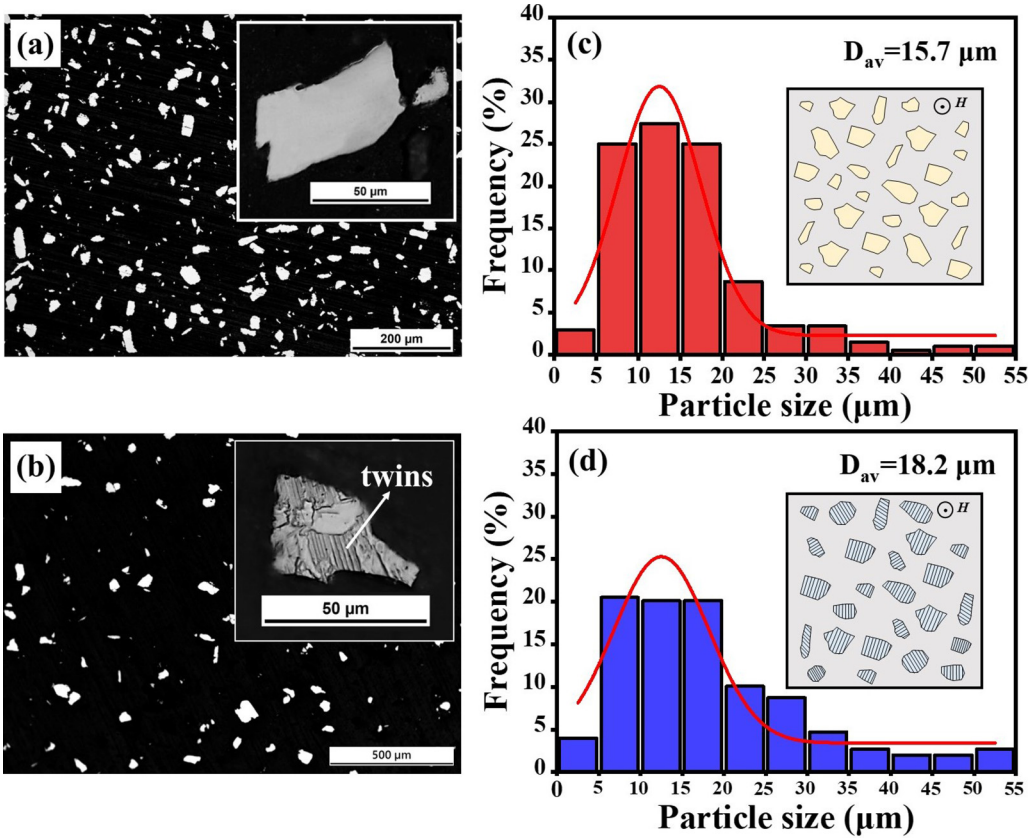

FIG. 2. (a,b) Morphologies of the bonded magnets using the (a) twin-free particles and (b) twinned particles by optical microscopy; the inset figures are the enlargement of a corresponding particle. (c,d) Distribution of the particle sizes of (c) twin-free and (d) twinned magnets; the inset in each figure is the schematic figure of the microstructures of the corresponding magnet.

evolution of magnetic domain structure during the magnetization and demagnetization processes was observed in an Evico Magnetics magneto-optic Kerr effect (MOKE) microscope and JEOL 2100F Lorentz transmission electron microscope (LTEM).

III. RESULTS AND DISCUSSION

A. Influence of twin structure on extrinsic magnetic properties

Figures 2(a) and 2(b) show the microstructure of twin-free and twinned textured MnAl powders; the axis of texture is perpendicular to the observation plane. All fragments are uniformly distributed in the epoxy matrix without inhomogeneous local aggregation. Figures 2(a) and 2(b) also show that the twin-free and twinned microstructures are still inherited from the original bulks after milling. The schematic figures of the microstructures of the two magnets are inset in Figs. 2(c) and 2(d). It is well known that the magnetic properties are sensitive to the particle size (grain size) in permanent magnets [30,31]. In this work, both magnets have approximately equal particle size, as proven by the particle size distribution curves in Figs. 2(c) and 2(d). Therefore, we can unequivocally compare the coercivity of twinned and twin-free particles 10–15 μm in size.

Figures 3(a) and 3(b) compare the room-temperature hysteresis loops of twin-free and twinned MnAl magnets measured along two directions: parallel and perpendicular to the external magnetic field. The local enlargement figures within the range from −1200 to 1200 kA/m are shown, and the coercivity as well as the remanence ratio of the magnets are summarized in Table I. It is obvious that the coercivity is rather sensitive to the presence of twin structures. The coercivities of the twin-free magnet are $H_{C//} = 200$ kA/m and $H_{C\perp} = 277.6$ kA/m, corresponding to the directions of parallel and perpendicular to the external magnetic field. The values are both approximately two times larger than those of a twinned magnet with $H_{C//} = 105.6$ kA/m and $H_{C\perp} = 146.4$ kA/m. Moreover, the coercivity of our twin-free magnet is almost two times higher than that of twinned melt-spun ribbons with the grain size of ∼2 μm, and it even approachethat of ball-milled Mn-Al-C powders with subcrometer particles (about 240–320 kA/m [27,32–35]). The comparison directly reveals that the elimination of twin structures is significantly beneficial to coercivity. Both of the hysteresis loops from −4.8 to 4.8 MA/m of twinned and twin-free magnets are shown in the insets in Figs. 3(a) and 3(b). The two magnets show similar magnetization behavior under high external magnetic field, and the hysteresis loops along and perpendicular to the texture direction are indistinguishable beyond 4 MA/m.

Besides the coercivity, the twin structures are also unfavorable to the remanence performance and anisotropy. Based on the shape of hysteresis loops and data shown in Table I, it is worth noting that the remanence can be dramatically enhanced via the elimination of twin structure. The remanence of a twin-free magnet is ∼ 70 A m^2/kg along the parallel direction, nearly 60% larger than 44 A m^2/kg of the twinned

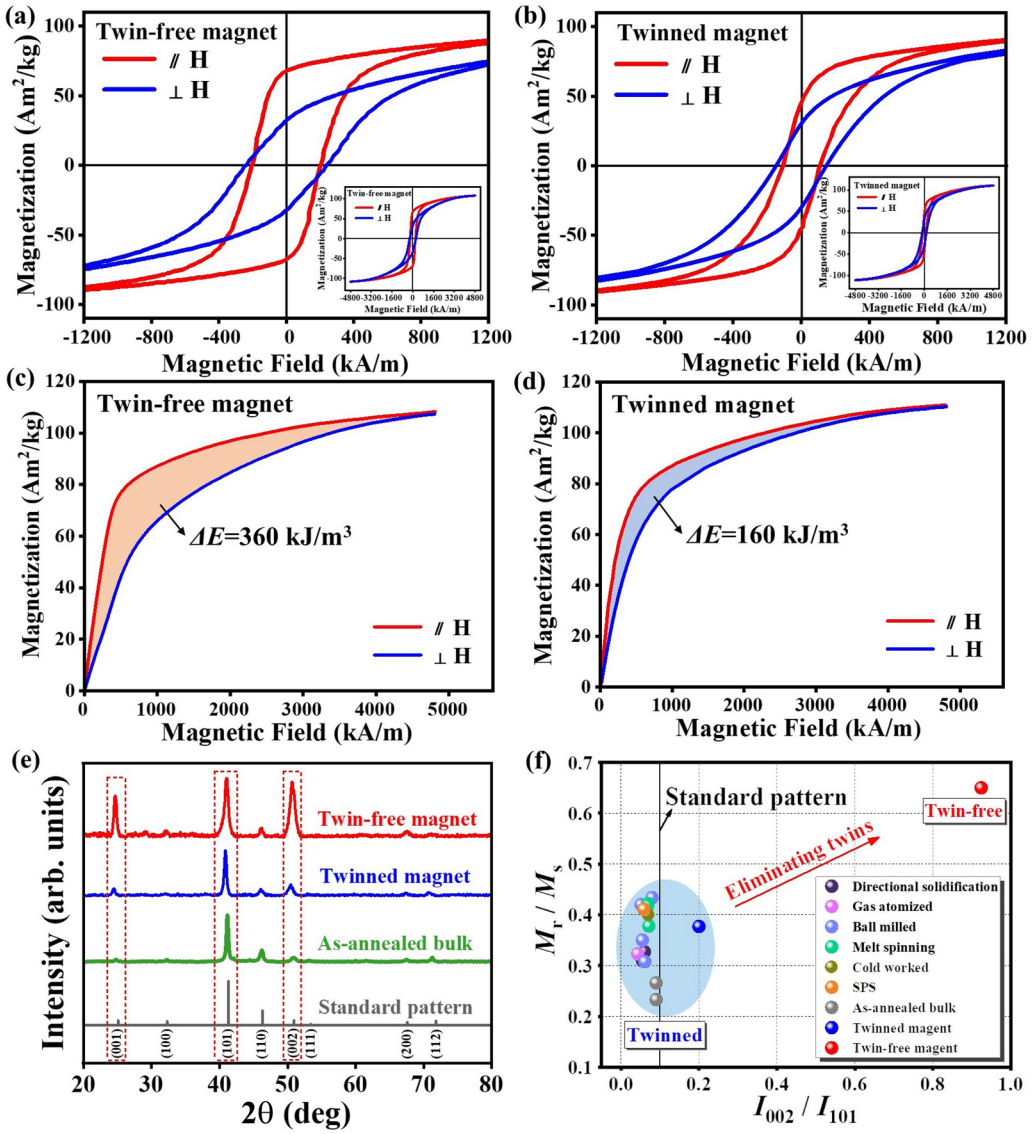

FIG. 3. (a,b) Magnetic hysteresis loops of (a) twin-free magnet and (b) twinned magnet, measured along and perpendicular to the direction of texture at 300 K. (c,d) Initial magnetization curves of (c) twin-free magnet and (d) twinned magnet, measured along and perpendicular to the texture at 300 K. (e) The room-temperature XRD patterns of the cross-section surface of twin-free and twinned magnets; the XRD patterns of the isotropic as-annealed bulks and standard pattern of the $L1_0$ phase are also added for comparison. (f) The comparison of crystallographic orientation and remanence ratio of the MnAl magnets obtained in this work with literature data [31,32,35,37–41].

magnet. The twin-free magnet shows relatively strong texture, while the twinned magnet shows almost isotropic behavior, which is also demonstrated by the difference in energies of magnetic anisotropy (the area of the region bounded by the magnetization curves along parallel and perpendicular directions) in the initial magnetization curves; see Figs. 3(c) and 3(d).

TABLE I. Coercivity and remanence ratio of the twinned and twin-free magnets along different directions.

	Twin-free	Twinned
$H_{c//}$ (kA/m)	200	105.6
$H_{c\perp}$ (kA/m)	277.6	146.4
$M_{r//}/M_s$	0.63	0.38
$M_{r\perp}/M_s$	0.30	0.24

Room-temperature XRD patterns of the twin-free and twinned magnets, and for comparison, the standard pattern and the pattern of isotropic twinned as-annealed bulk alloy, are also depicted in Fig. 3(e), in order to show the effect of twin structure on the magnetic anisotropy in $L1_0$-MnAl magnets [36]. The twin-free magnet has a strong [001] texture which is reflected by the relatively high intensity of (001) and (002) peaks, while for the twinned magnet and isotropic twinned bulk, the relative intensities of the peaks are basically in accordance with those of the standard pattern, indicating that almost no preferred orientation is realized in the twin-containing MnAl alloys. This result also supports the shape of

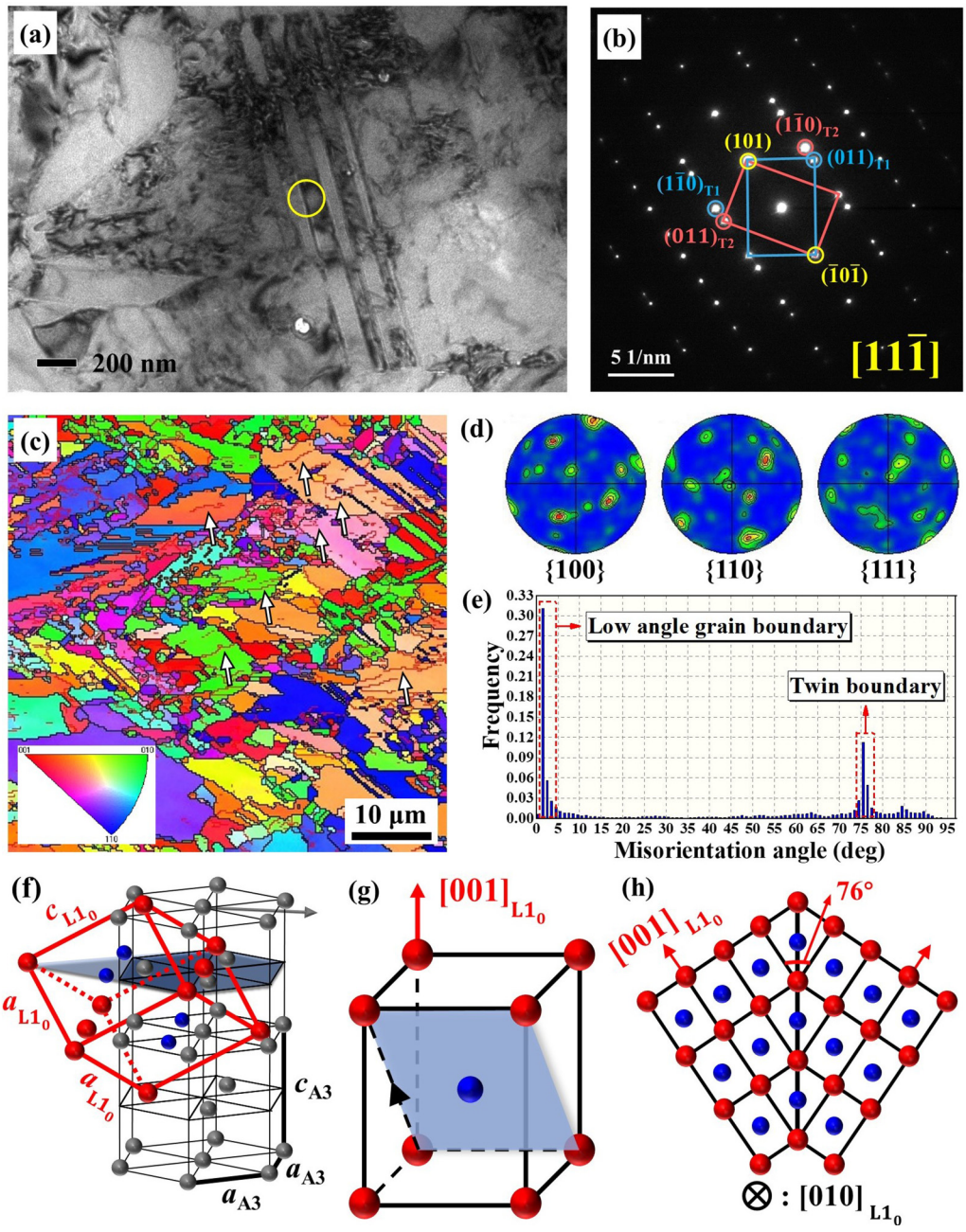

FIG. 4. (a) TEM image showing the morphology of twin structures of MnAl alloys. (b)The SAED pattern of the twin structure. (c) EBSD map of as-annealed $L1_0$-MnAl. (d) Pole figure of as-annealed $L1_0$-MnAl from three different crystallographic axes. (e) Histogram of misorientation angle. (f) Crystallographic phase relations between high-temperature $A3$ phase and low-temperature $L1_0$ phase [19]. (g) The twinning plane in $L1_0$ MnAl alloys. (h) A schematic figure showing the atomic distribution nearby a twin boundary. It should be mentioned that we only show the condition that the atomic ratio Mn:Al=1:1 for convenience.

the *M-H* hysteresis loops and the initial magnetization curves. Here we use the intensity ratio of I_{002}/I_{110} to visually reveal the orientation degree of these magnets, as shown in Fig. 3(f). The value significantly increases from 0.09 for twinned bulk and 0.20 for a twinned bonded magnet to 0.93 for twin-free magnet.

We summarize I_{002}/I_{110} and the remanence ratio of MnAl magnets prepared by multiple methods including annealing, directional solidification, ball milling, melt spinning, spark plasma sintering, cold working, gas atomization, etc., in Fig. 3(f) [31,32,35,37–41]. As one can see, all of the twinned magnets show relatively low values of I_{002}/I_{110} together with weak remanence. Thus, the preferred [001] orientation accompanied by much higher remanence is realized only in a twin-free magnet via the elimination of twin structure. Therefore, the existence of twin structure is a critical factor which prevents the achievement of high remanence in MnAl magnets. The relevant mechanism is discussed in the Supplemental Material [7].

To uncover the microstructure of twins, TEM analysis was performed, as displayed in Fig. 4(a). Obvious stripe-shaped lamella morphologies indicate the twin structures in the al-

loy. The crystal structure of the twins was analyzed by an electron diffraction (SAED) pattern [the yellow circle region in Fig. 4(a)] with the electron beam direction is along the $[11\bar{1}]$, axis of L10-phase as shown in Fig. 4(b). The twinning plane is detected to be (101), which is in agreement with the observation from Palanisamy *et al.* [17] and Müllner *et al.* [19]. It should be mentioned that we have collected the SAED patterns from over ten regions which have twins, and (101) orientation of the twinning plane is well reproducible.

EBSD images were adopted to further characterize the microstructure in twinned MnAl alloy, as shown in Fig. 4(c). The pole figures from different crystallographic directions in Fig. 4(d) indicate the isotropic feature in the twinned sample, in accordance with the XRD patterns. In Fig. 4(c), obvious twin structures with straight twin boundaries can be seen; also some red lines with negligible difference in crystallographic orientation between the two sides of the lines could be detected, as marked by white arrows. According to the histogram of the grain misorientation angle in Fig. 4(e), the grain misorientation angles concentrate on two regions: 1°–3°, representing the small angle grain boundaries which are shown as red short lines in Fig. 4(c); and 74°–77°, representing the twin boundaries.

Based on the above results, the structure of the twins in $L1_0$-MnAl can be established by analyzing the orientation relationship between the parent $A3$ phase and the $L1_0$ phase. According to the shearing mode of $A3 \rightarrow L1_0$ phase transformation raised by Müllner *et al.* [19], the relationship between $A3$ phase and $L1_0$ phase could be expressed in Fig. 4(f). The habit plain is (101), and the shearing directions are sixfold equivalent $\langle 101 \rangle$ directions, as indicated in Fig. 4(g). Therefore, the schematic two-dimensional figure (viewing from the [010] direction) of the twin structure can be plotted, as shown in Fig. 4(h). Based on the XRD pattern, the lattice parameter of the $L1_0$ phase could be calculated to be $a = 0.277$ nm, $c = 0.354$ nm. Therefore, the easy magnetization [001] axes of the adjacent twin variant form an included angle of about 76°, which perfectly fits the EBSD results. This included angle of [001] axes in twin structures is the key factor in preventing the realization of high remanence in permanent-magnetic alloys with $L1_0$ lattice structures. Meanwhile, twin structure locally deteriorates the anisotropy of the bulk $L1_0$-MnAl, which is partly responsible for the decline of coercivity and will be discussed as follows.

Although numbers of works focus on the twin structure in $L1_0$ magnets, the coercivity is derived from the twin structure. To uncover the mechanism, the interaction between the twin structure and the magnetic domains during magnetization and demagnetization processes were analyzed by *in situ* MOKE images, as shown in Fig. 5. It is obvious that twin variants can be observed via light and shade contrast in all the MOKE images, and the morphology of the domain structure can be seen inside the variants with a weaker contrast. Figures 5(a)–5(i) correspond to the data points 1–9 on the magnetization and demagnetization curve of Fig. 5(j). Figure 5(a) shows the initial magnetic domain structure with stripe magnetic domains, and the direction of the applied external magnetic field is marked by a yellow arrow in the bottom part of Fig. 5(a). With the application of magnetic field, the domain wall propagation starts from one twin boundary of the twin variants, as indicated by the yellow arrows in Fig. 5(b). As the external field increases, the domain walls depart one side of the twin boundaries and propagate to the other twin boundary of the variants. The domain wall propagation has been finished when the magnetic field reaches 277.68 kA/m, according to the criterion of homogeneous color in each variant, as shown in Fig. 5(d). During the backward demagnetization process from the saturation state, the prior location for the reversed domains' nucleation is also the twin boundary, as marked by the yellow arrow in Fig. 5(e). As the magnetic field further reduces, the domain wall propagation and new reversal domains from twin boundaries can be observed clearly in Fig. 5(f). Afterwards, more reversal domains nucleate and grow up from the twin boundaries to the inner part of each variant. When the external magnetic field drops to 0 kA/m, the magnetic domain structure recovers to the initial state, as shown in Fig. 5(i).

In order to highlight the evolution of magnetic domains, local enlargement sketches of a certain region inside the yellow rectangle in Figs. 5(a)–5(i) are shown in Fig. 5(k), 1–9, which overlook the contrast between the twin variants and can clearly demonstrate the contrast of magnetic domains without distortion. The gray line stands for the twin boundary and these figures clearly indicate the effect of twin boundary on the magnetic domain nucleation during the magnetization reversal process. Figure 5(l) schematically explains the reason for four-color contrast in the domain morphologies in Figs. 5(a)–5(i). Without applying an external magnetic field, easy axes in the two adjacent twin variants have an included angle of ∼76°, resulting in four types of 180° domains with different spontaneous magnetization directions. This is the reason why we can observe four different gray scale contrasts in the MOKE images. With the increasing of the magnetic field, the domain wall motion process is triggered in priority. Therefore, in each twin variant, the domains with the easy axes closer to the external field [yellow and red areas in Fig. 5(i)] are energetically preferred and they tend to grow up. Inversely, the remaining two types of domains gradually shrink. When the external field is $H = 277.68$ kA/m, each twin variant has a homogeneous color, because the "preferred" domains have occupied the whole variants with uniform magnetization direction; this results in two-color contrast in Fig. 5(d). However, this field is still far away from the anisotropy field which is over 3.2 MA/m. It means that this field provided by MOKE microscopy is insufficient to complete the domain rotation process, so the easy axes of the domains in the adjacent twins are still not uniformly aligned along the external field. Therefore we can still observe two different colors in Fig. 5(d).

For multiscale investigation of the interaction between the twin boundaries and magnetic domains, the observation of magnetic domains was carried out by Lorentz TEM. The maximum external magnetic field reaches 80 kA/m, but the severe astigmatism affects the observation when the external field is larger than 48 kA/m; therefore only the figures of the magnetic field below 48 kA/m appear here. Microstructure and *in situ* evolution of magnetic domains are shown in Figs. 6(a)–6(h); these figures correspond to the points 1–8 on the curve in Fig. 6(i), with the magnetic field direction indicated by the yellow arrow in Figs. 6(a) and 6(e). In order to illustrate the interaction between the twin boundary and the domain wall,

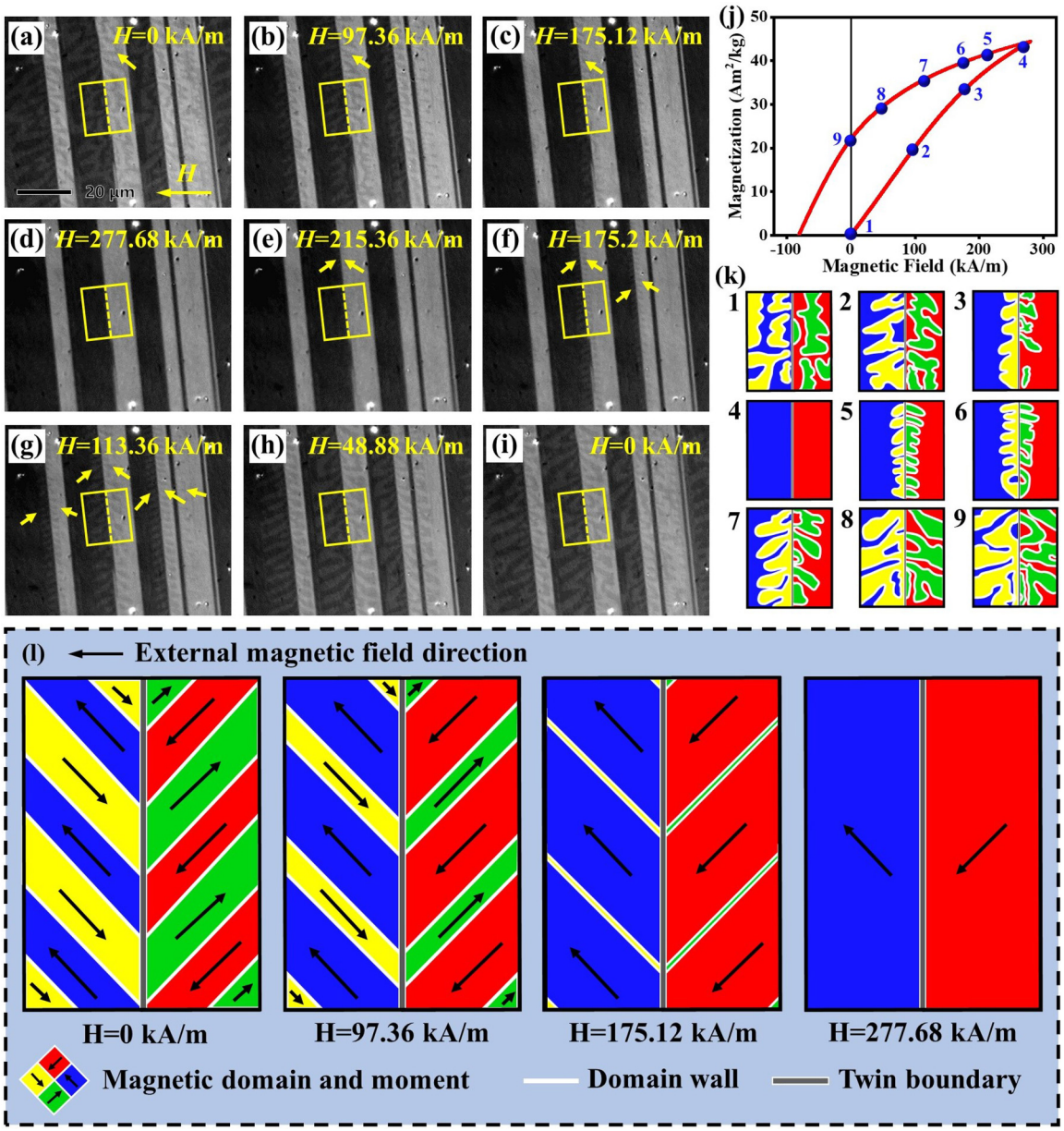

FIG. 5. (a–i) MOKE images showing the interaction of domain structures and twin boundaries during magnetization and demagnetization processes in twinned MnAl alloys. (j) Magnetization and demagnetization curve under the MOKE observation condition. (k) Schematic figures of magnetic domain evolution selected from the yellow rectangle in the MOKE images, corresponding to the data points 1–9 on the curve. (l) Schematic figures explaining the color contrast in the MOKE images and the evolution of domain structure during magnetization process.

the schematic diagrams of magnetic domain evolution process are shown in Figs. 6(j) and 6(k). These sketches are made for the regions of Figs. 6(a)–6(h) inside the yellow rectangles, and the dotted lines correspond to the twin boundaries. Figure 6(j) shows the magnetization process with the growth of domains along the twin boundary (green line). When the magnetic field is 16 and 32 kA/m, the extension of the domains is tiny, while a huge leap occurs when the magnetic field reaches 48 kA/m; however, the magnetic domains in other areas far away from twin boundaries do not move. The backward demagnetization process is shown in Fig. 6(k) (the morphology under −8 kA/m does not change compared with 0 kA/m; therefore only points 5, 7, and 8 are shown here). When the magnetic field increases to −16 kA/m, remarkable changes have taken place, which indicates the growth of reversal magnetic domains near the twin boundary. It is worth noting that the direction of the domain wall movement is always perpendicular to the twin boundary, and it is independent of the direction of the external magnetic field. Hence, the interaction area between the twin boundary and domain wall occurs in the white circles in Figs. 6(j) and 6(k), which show very weak pinning and strong nucleation effects, and this is consistent with the results illustrated by micromagnetic simulation [26].

According to these *in situ* MOKE and Lorentz TEM images, the twin boundaries are demonstrated to act as an initial site for magnetic domain nucleation during the demagnetiza-

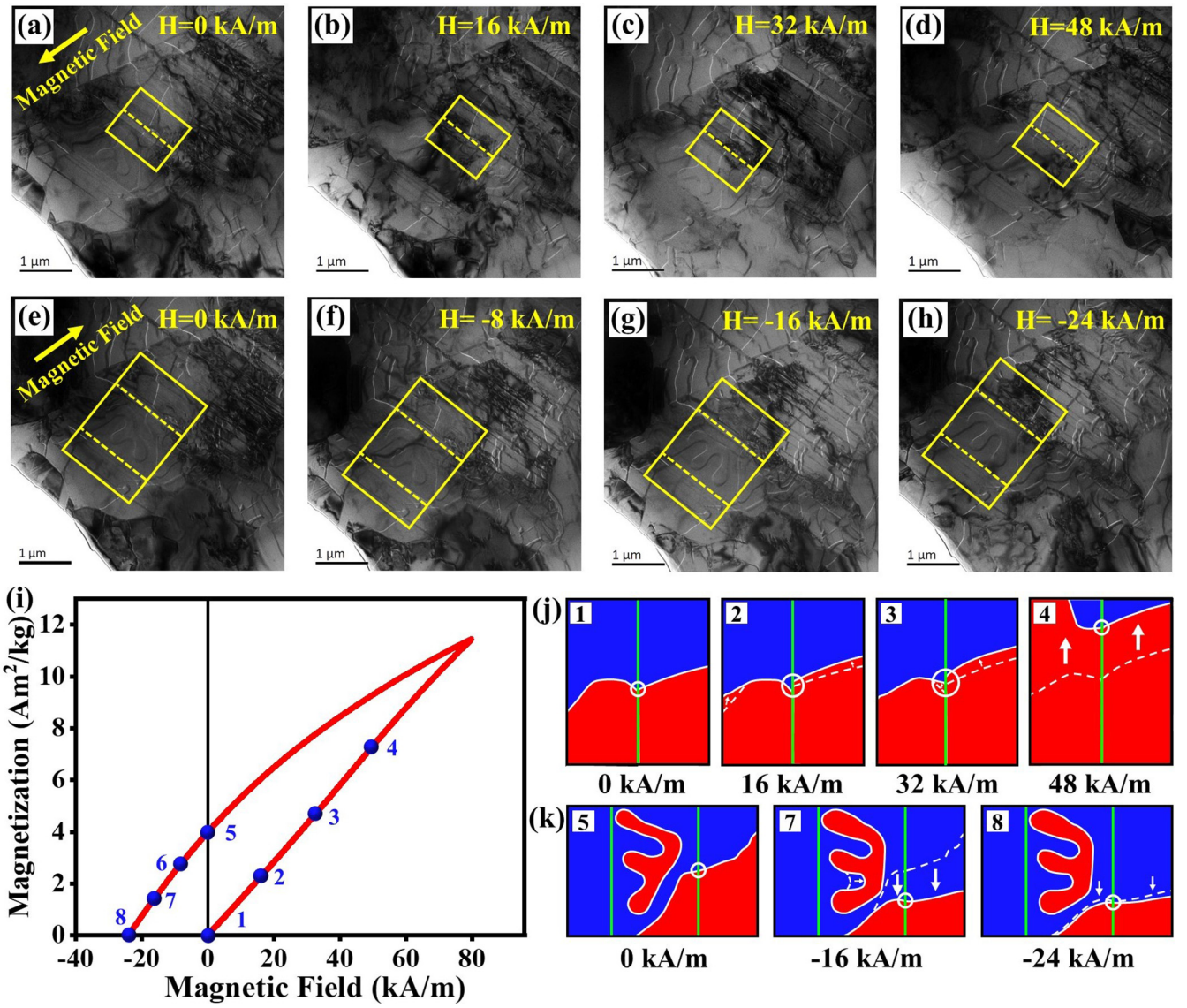

FIG. 6. (a–h) Lorentz TEM figures showing the magnetic domains and microstructures during magnetization and demagnetization processes in twinned MnAl alloys. (i) Magnetization and demagnetization curve under the LTEM observation condition. (j,k) Schematic figures of magnetic domain evolution of the region of yellow rectangles in LTEM figures during the (j) magnetization and (k) demagnetization process selected from and corresponding to the data points 1–8 on the hysteresis loop.

tion process, reducing the coercivity of MnAl magnets. This observation can be extended from $L1_0$-MnAl to other $L1_0$ permanent magnets, where the twin structure plays a similar role, resulting in a negative effect on the coercivity, which is similar to the strain effect in the study of Yi *et al.* [42] and the inhomogeneous grain structure investigated by Schrefl *et al.* [43] on the coercivity. Klemmer *et al.* [8] and Vlasova *et al.* [22] predicted the degradation of coercivity in FePd, CoPt, and FePt $L1_0$ alloys may be induced by the high-density twin structure. Here we acquire the direct and credible evidence of the negative role of twins in $L1_0$-MnAl alloys. Moreover, in some other hard magnetic systems such as rare-earth-based permanent magnets, the twin structure can also play a similar role. The "twinlike" structure in 1:12-NdFeTi alloys is also indicated to be the nucleation center during the reversal process, and accounting for attenuation of the coercivity [44]. Meanwhile, no proof about the pinning effect of twin structure has been observed. Hence, the twin structures promote the nucleation of reversal magnetic domains rather than improve the coercivity by the weak pinning effect. Bance *et al.* [26] provided a similar conclusion indicating that the angle between adjacent variants' easy magnetization axes as well as the angle between the easy magnetization axis and applied field facilitates the formation of the domain wall rather than the uniform state. In addition, the nucleation field will never be lower than the field required to depin the domain wall from the twinning region according to the calculation, called weak pinning and strong nucleation, therefore degrading the coercivity of $L1_0$-MnAl magnets.

B. Effect of dislocation on the coercivity and the mechanism

As reported in the previous section, $L1_0$-MnAl demonstrates a typical nucleation mechanism of coercivity [45]. In

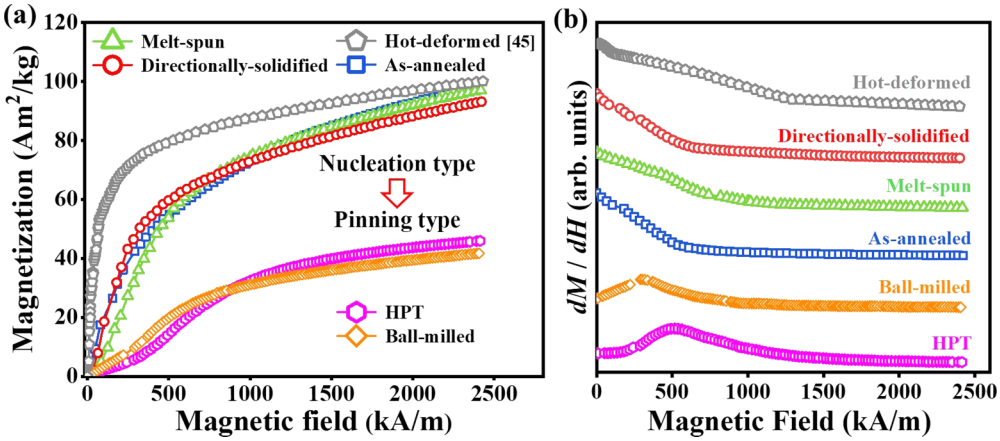

FIG. 7. (a) Initial magnetization curves of melt-spun ribbon, directionally solidified bulk, hot-deformed sample [46], as-annealed bulk, ball-milled powders, and HPT specimens along random directions measured at 300 K. (b) dM/dH curves of samples in (a), showing the nucleation or pinning mechanism of coercivity.

Fig. 7(a), the initial magnetization curves of several typical MnAl magnets including melt-spun ribbons, directionally solidified specimen, hot-deformed bulk [46], and as-annealed samples, are shown. All these preparation processes, phase composition, grain size, defect types, and coercivity mechanism are described in detail in Table II. The grain sizes of these types of magnets are generally larger than the critical single domain size of 773 nm [46]. The corresponding dM/dH curves of magnetization curves are depicted in Fig. 7(b). A typical signature of the nucleation mechanism is high initial magnetic susceptibility when the samples are magnetized from the thermally demagnetized state. For the hot-deformed, directionally solidified, melt-spun, and annealed samples, the maximum of dM/dH appears at low field, and the coercivity is generally lower than 240 kA/m. However, peak values of dM/dH of the ball-milled and high-pressure-torsion samples appear at much higher fields (320–480 kA/m), indicating the strong pinning effect with the consideration that the grain size of ball-milled and high-pressure-torsion MnAl magnets is over 500 nm or even reaches several micrometers according to the extension length of twin strips, which is larger than the critical size of single domain. As a result, these samples can have much higher coercivity of 320–400 kA/m than the nucleation-dominated samples. Therefore, it is

TABLE II. The preparation process, phase composition, grain size, defect types, and coercivity mechanism of melt-spun ribbon, directionally solidified bulk, hot-deformed sample [46], as-annealed bulk, ball-milled powders, and HPT specimens.

Preparation methods	Description of preparation process	Phase composition	Grain size (μm)	Defect types	Coercivity mechanism
Hot deformed [46]	1. Induced melting 2. 1100 °C for 2 days 3. Hot extracted at 680 °C	$L1_0$ and small amount of β	1–20	Twins	Nucleation
Directionally solidified	1. Vacuum arc melting 2. Cast as a φ7 rod 3. Bridgman directional solidification	$L1_0$	50–200	Twins	Nucleation
Melt spun	1. Vacuum arc melting 2. Melt spinning 3. 500 °C for 12 min	$L1_0$	2–10	Twins	Nucleation
As annealed	1. Vacuum arc melting 2. 1050 °C for 10 h 3. 500 °C for 15 min	$L1_0$	200	Twins	Nucleation
Ball-milled	1. Vacuum arc melting 2. 1050 °C for 10 h 3. 500 °C for 15 min 4. Ball milling for 2 h	$L1_0$	1–5	Twins and dislocations	Pinning
HPT	1. Vacuum arc melting 2. 1050 °C for 10 h 3. 500 °C for 15 min 4. HPT under 5 GPa	$L1_0$	0.5–10	Twins and dislocations	Pinning

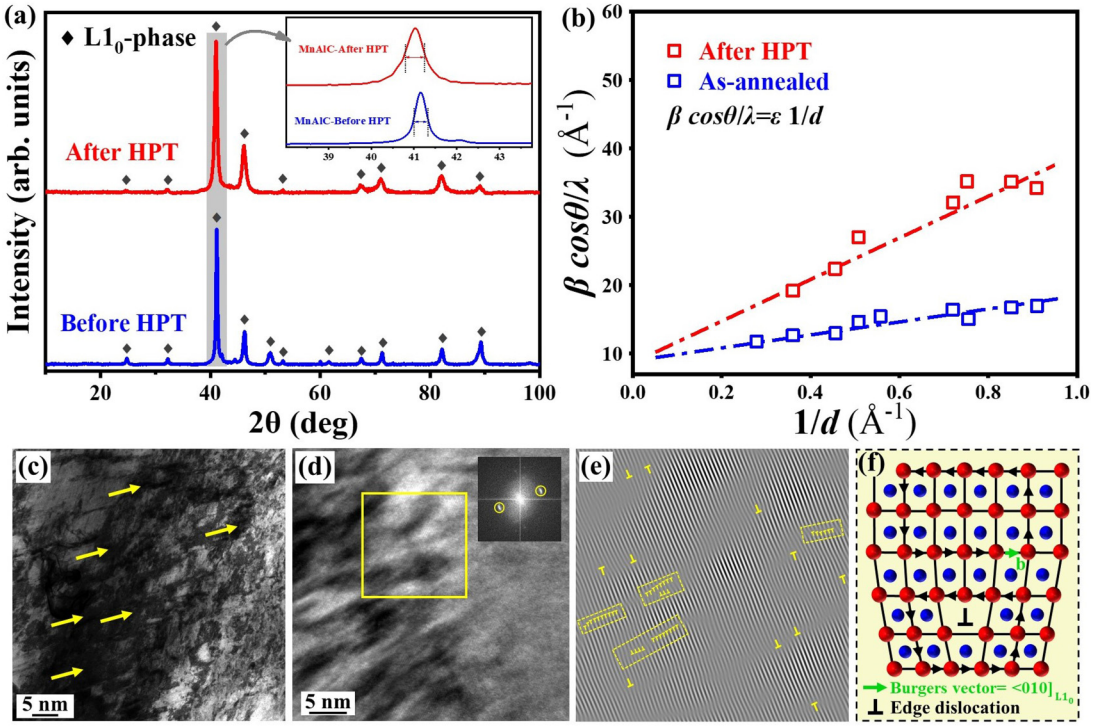

FIG. 8. (a) The room-temperature XRD patterns of $L1_0$-MnAl before and after HPT deformation. (b) The lattice strain analysis based on the method of Williamson and Hall [49]. (c) TEM image showing the dislocation morphology of $L1_0$-MnAl after HPT deformation. (d) High-resolution image of $L1_0$-MnAl after HPT deformation, and the FFT pattern of the area in the yellow square is shown in the inset. (e) Image after inverse FFT operation, indicating high density of dislocations. (f) Schematic graph showing the lattice structure of dislocation in $L1_0$-MnAl alloys.

necessary to introduce a new pinning center in the system to improve coercivity.

For $L1_0$-MnAl alloys, the domain wall width could be calculated by the equation as follows:

$$\delta_w = \pi\sqrt{\frac{A}{K}}. \tag{1}$$

The exchange stiffness constant A is determined to be $2.42 \times 10^{-11}\,\mathrm{J/m^3}$ in Ref. [46]; the magnetocrystalline anisotropic constant K of $L1_0$-MnAl is $1.53\,\mathrm{MJ/m^3}$, as summarized in Table S1 of the Supplemental Material [7]. Using Eq. (1), the domain wall width is calculated to be 12.49 nm. According to domain wall pinning theory, the pinning defects should be of the size of δ_w [45]. Zhao *et al.* [47] proved that significantly enhanced coercivity could be realized by introducing the nanoprecipitates with a size smaller than 20 nm. For this reason, dislocation could be a suitable candidate to act as a pinning center, because they can be easily obtained and controlled by deformation and annealing treatment. As displayed in Table II, the magnets with only twin defects show a nucleation type coercivity mechanism, while the appearance of dislocations can induce a strong pinning effect inside. Ball-milled powders show pinning characteristics to some degree with a pinning field of about 320 kA/m [see Fig. 7(b)], which could be attributed to severe plastic deformation. Moreover, the MnAl magnet, which was obtained by high-pressure torsion (HPT, reveals an even stronger pinning effect with a field of nearly 480 kA/m. Therefore the HPT-MnAl alloys were selected as the object to analyze the impact of dislocation structure on the magnetic properties and the corresponding mechanism.

The XRD patterns of the $L1_0$-MnAl before and after HPT deformation are shown in Fig. 8(a). No decomposition happens during the deformation process, and the local enlargement of the patterns indicates the broadening of the diffraction peaks, which suggests high density of strain after HPT; besides, the peak left shift is attributed to the macroscopic residual stresses, leading to the contraction of the crystal lattice [48]. For illustrating the appearance of lattice strain induced by HPT of samples directly, the Williamson and Hall method was employed [49], which obeys the equation as

$$\beta\frac{\cos\theta}{\pi} = \varepsilon\frac{1}{d}, \tag{2}$$

where β is the ratio of XRD peak area and height, θ is the scanning angle, and λ represents the wavelength of the x ray. On the right side, ε means the internal lattice strain and d is the interplanar spacing. Figure 8(b) shows the $\beta\cos\theta/\lambda$–$1/d$ curves of $L1_0$-MnAl before and after HPT, of which the slopes indicate the magnitude of lattice strain. It is obvious that there is a higher density of strain in the lattice of $L1_0$-MnAl after HPT. To clarify the existence of the lattice strain, the micromorphology and high-resolution images were obtained by TEM, as shown in Figs. 8(c) and 8(d). Ultrahigh density of dislocation nets could be observed in the HPT sample as seen by the dark contrast in Fig. 8(c). Figure 8(d) is the corresponding TEM image, but the resolution is insufficient to obtain information about the lattice, owing to the severe deformation.

In order to get a better view, fast Fourier transform (FFT) and inverse FFT (IFFT) were employed in the area enclosed by a yellow square. The FFT pattern is displayed in the top right of Fig. 8(d) and the only two diffraction spots that could be recognized are selected for the IFFT image. The IFFT image is shown in Fig. 8(e); the lattice fringe is clearly visible because other contrast information is eliminated during the IFFT process. A large amount of dislocations and lattice distortion defects can be recognized and most of the dislocations are marked out by "T"-like symbols. It can be recognized that the scale of the distortion region affected by dislocations is 1–10 nm, which is close to the width of the domain wall in $L1_0$-MnAl. Moreover, the distance between two dislocations is also lower than 10 nm, which is far away from 100 nm in other metallurgical states [38], indicating an ultrahigh density of dislocations in HPT-MnAl, and can be responsible for a strong pinning effect. Moreover, several dislocations gather into some areas as displayed in the yellow dashed rectangles, explaining the source of large lattice strain of HPT-MnAl. The atomic structure diagram of dislocations in $L1_0$-MnAl alloys are plotted in Fig. 8(f), in which the Burgers vector $\boldsymbol{b}$ is $<010]$.

A series of low-temperature annealing treatments (200 °C, 250 °C, 300 °C, 350 °C, and 400 °C for 10 min, respectively) were made to regulate the density of the dislocations, in order to investigate the effect of dislocation on the magnetic properties. The low temperatures are selected in order to avoid the decomposition of the $L1_0$ phase and to form the different densities of the dislocations. Figures 9(a) and 9(b) show the XRD patterns of as-annealed HPT-MnAl specimens; no additional diffraction peaks appear in the pattern after the annealing treatment, indicating that no decomposition behavior takes place. Meanwhile, the right shift of the peaks signifies the reduction of the crystal lattice distortion generated from macroscopic residual stress.

In order to reveal the relationship between microstructure and annealing treatment, the microstructures and the corresponding schematic diagrams are illustrated in Figs. 9(c)–9(f). Two rows with indices 1 and 2 correspond to two types of observation areas. The first area is suitable for observing twin structure and the second one contains obvious grains and dislocations. In both rows, the figures from left to right correspond to the $L1_0$-MnAl before HPT (c), after HPT (d), HPT and annealed at 250 HPT deformation; the twin structure is apparent and easily distinguished in Fig. 9(c1). Almost no dislocation could be observed in the nondeformed sample, as exhibited in Fig. 9(c2). After HPT, the morphology of twin structure becomes "blurry" and illegible because of the deformation, as seen in Fig. 9(d1). In some areas, the reticulated structure which has black boundaries starts to appear, as marked by the yellow circle in Fig. 9(d2). These are detected to be the dislocation nets, indicating that severely plastic deformation does not change the phase composition, but introduces a high density of dislocations. After the low-temperature treatment of 250 °C for 10 min, twin laths become easier to distinguish than in the as-deformed state, as shown in Fig. 9(e1). Figure 9(e2) shows that the areas with black contrast decrease, indicating the reduction of dislocation density; furthermore, the morphology transforms from dislocation nets to dislocation cells, as marked by the yellow arrows and circles. The change of dislocation morphology illustrates that, under low-temperature treatment conditions, the migration and release of dislocations occur, but the processes are not completed. With the further increase of annealing treatment temperature up to 400 °C, twin structure becomes clearly visible, as shown in Fig. 9(f1). As seen in Fig. 9(f2), the dislocation cells disappear and only one dislocation wall can be observed, suggesting the much lower dislocation density. Dislocation distribution is schematically indicated in Figs. 9(d3)–9(f3), accompanied with a decreasing dislocation density.

For facilitating the analysis, quantifying the dislocation density of samples with different conditions is necessary; thus EBSD measurement was used. Figures 10(a1)–10(g1) show a set of Kikuchi patterns corresponding to different metallurgical states as marked in every figure. The resolution of Kikuchi patterns is directly related to the degree of order of the lattice, and the distortion of the crystal lattice reduce the sharpness of the pattern [38]. It is obvious that before HPT, the pattern is of high quality but after deformation, nearly no Kikuchi band can be recognized. Afterwards, with the increasing annealing temperature, the quality of Kikuchi patterns is gradually improved, so the quantitative dislocation density can be analyzed based on the sharpness of the Kikuchi patterns. Fast Fourier transformation (FFT) is a method for analyzing the sharpness of an image through converting the image to the frequency domain [50], and the results after FFT are displayed in Figs. 10(a2)–10(g2). The radii of the center of the bright spots are displayed in Fig. 10(h), indicating the quality of the patterns, where the higher quality is accompanied with larger radius and vice versa. The bright spots' radii are inversely proportional to the dislocation density, so the reciprocal of the radii are calculated in Fig. 10(i), indicating the relationship of the dislocation density of these different metallurgical states. For verification of the calculation results of dislocation density, a rough statistic of dislocations from TEM images is made and also shown in Fig. 10(i). The results of FFT calculation and TEM images statistics present the same tendency, which confirms the evaluation of dislocation density. It is clear that after HPT deformation, a large number of dislocations are presented in the sample. After annealing treatment, the density of dislocation gradually decreases with the increasing annealing temperatures. As a consequence, a series of $L1_0$-MnAl with different dislocation densities were obtained; the effect of dislocation on the magnetic properties has been studied based on these samples.

The evolution of magnetic properties with decreasing dislocation density is exhibited in Fig. 11. The room-temperature magnetization curves in Fig. 11(a) illustrate the variation in magnetization under 4 MA/m magnetic field ($M_{4\mathrm{MA}/m}$), from 51 A m^2/kg for the HPT sample to 90 A m^2/kg for the sample annealed at 400 °C. Since in $L1_0$-MnAl the magnetic ordering depends on the Mn-Mn ferromagnetic coupling, which is sensitive to the Mn-Mn distance [1], dislocations can introduce the lattice distortion, leading to a higher possibility of antiferromagnetic coupling between local Mn-Mn atom pairs. This results in the monotonous increase of magnetization under 4 MA/m with the reduction of dislocation density.

The dM/dH curves have a maximum at ∼480 kA/m, that corresponds to the pinning field, as displayed in Fig. 11(b). Two pinning models have been developed to reveal the pin-

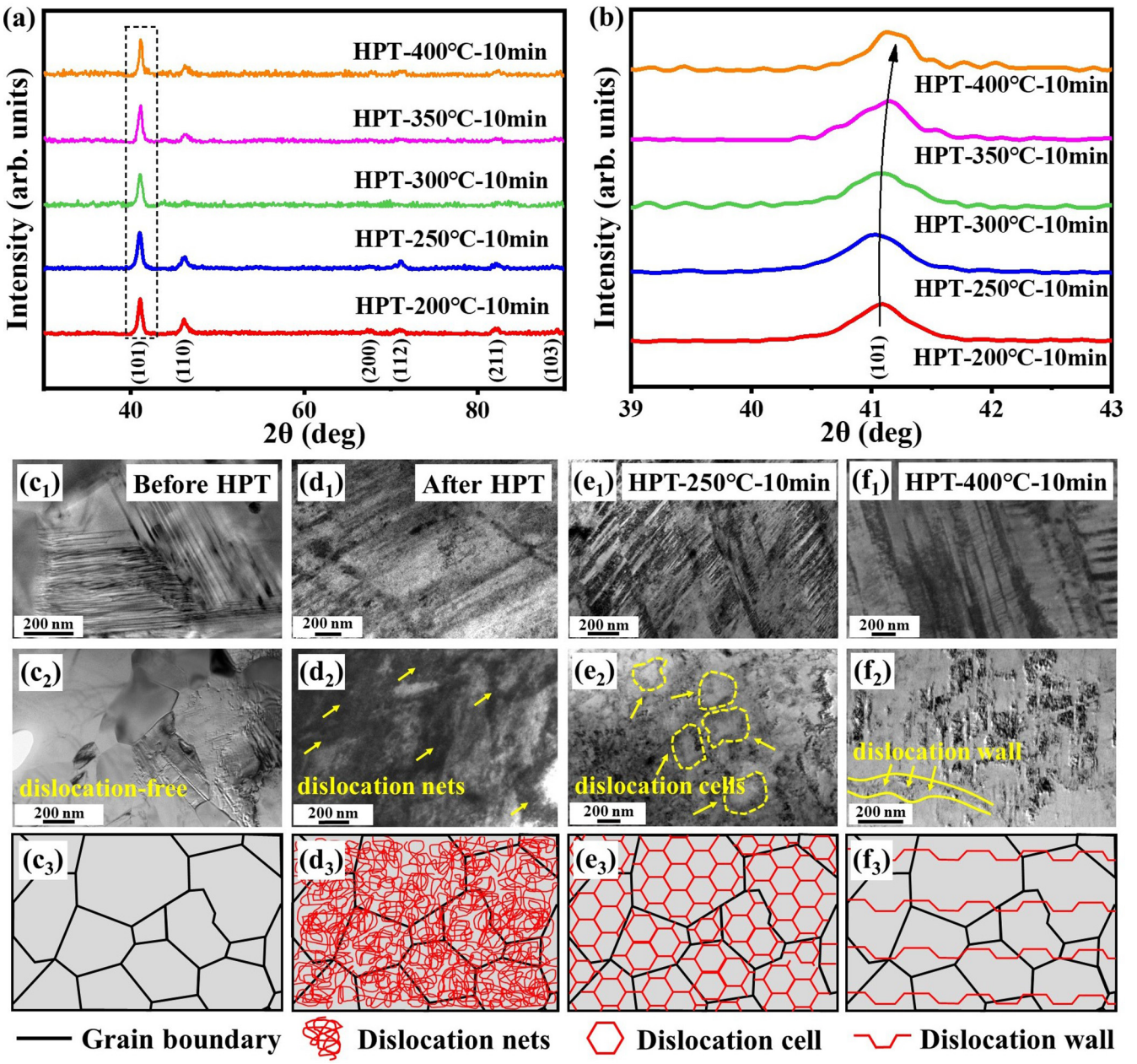

FIG. 9. (a) The room-temperature XRD patterns of HPT-MnAl after a series of annealing treatment for 10 min under 200 °C, 250 °C, 300 °C, 350 °C, and 400 °C. (b) The enlargement of the (101) peak of (a) in the dashed rectangle. (c_1−f_1): TEM images of twin structure evolution in $L1_0$-MnAl before HPT, after HPT, annealed for 10 min under 250 °C, and annealed for 10 min under 400 °C. (c_2−f_2): TEM images showing the dislocation morphology in $L1_0$-MnAl before HPT, after HPT, annealed for 10 min under 250 °C, and annealed for 10 min under 400 °C. (c_3−f_3): Schematic figures of the dislocation morphology corresponding to (c_2−f_2), respectively.

ning mechanism, which are called strong pinning and weak pinning, respectively [51]. Strong pinning means that under the magnetic field close to H_{pin}, the pinned domain wall starts to move through a pinning site and will then be pinned by another one (this is also called "pin by pin"). For weak pinning, the domain walls will break away from all the pinning sites simultaneously when the magnetic field reaches the critical value. Evidently, the strong pinning mechanism is closely correlated to the density of the pinning site, while weak pinning is mainly decided by the pinning force of a single pin and the range of interaction between the domain wall and pinning site.

The comparison in pinning field of these samples with different dislocation densities, shown in Fig. 11(b), indicates that dislocation is likely to present strong pinning function instead of weak pinning. Figure 11(c) shows the hysteresis loops of the HPT and annealed samples. The obtained coercivity and magnetization, as well as the density of dislocation, are summarized in Fig. 11(d). It is worth noting that the dislocation density of the HPT MnAl magnet is set as the standard value of 100%; the relative dislocation densities of other annealed samples were calculated based on the standard value. The coercivity of the HPT MnAl magnet which contains the dislocation nets is 424 kA/m. With the decreasing

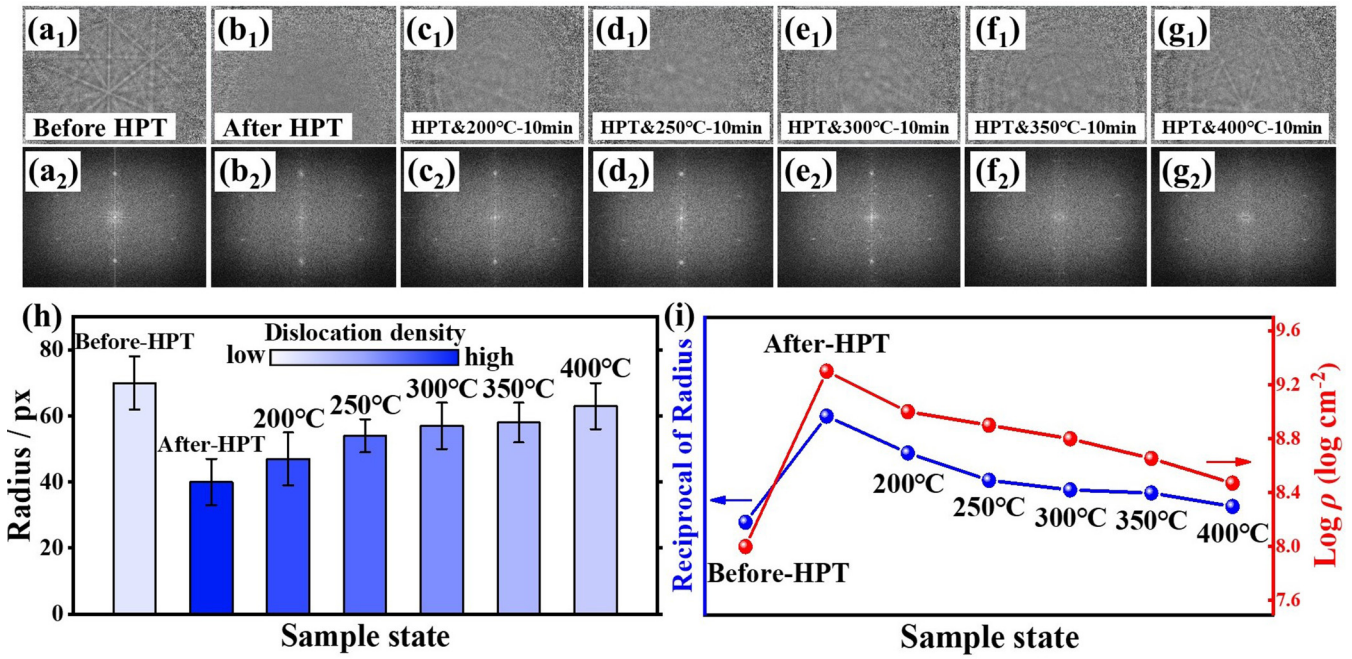

FIG. 10. (a_1-g_1) Kikuchi patterns of the samples before HPT (a_1), after HPT (b_1), and annealed for 10 min under 200 °C (c_1), 250 °C (d_1), 300 °C (e_1), 350 °C (f_1), and 400 °C (g_1). (a_2-g_2) Images after FFT of Kikuchi patterns corresponding to (a_1-g_1), respectively. (h) Radius of the center of bright spots in the FFT images for different sample states. (i) Reciprocal of radius of the center spots in the FFT images and the dislocation density of samples.

density and varied configuration of the dislocations, the coercivity is gradually reduced to 400, 384, 344, and finally to 328 kA/m. Compared with MnAl magnets prepared by other methods, the lowest coercivity in these samples still possesses strong competitiveness and the magnetization is much higher, indicating dislocation to be a kind of positive defect. The correlation between coercivity and dislocation density also supports the strong pinning model. In addition, the MOKE images of the annealed bulk and HPT MnAl magnets shown in Fig. S3 in the Supplemental Material [7] also support these

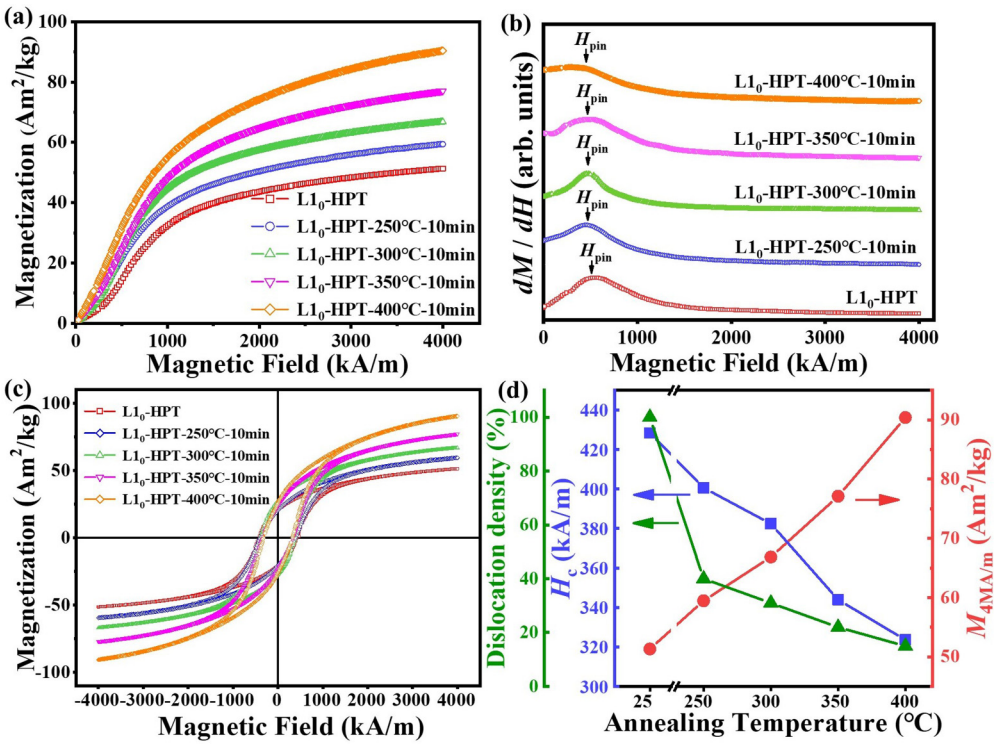

FIG. 11. (a–c) Initial magnetization curves (a), dM/dH curves (b), and hysteresis loops (c) of $L1_0$-MnAl after HPT and series of annealing treatment. (d) Evolution of dislocation density, H_c and $M_{4\ \mathrm{MA}/m}$ with the different annealing treatment temperature.

results. Under these circumstances, dislocation with a positive effect should be introduced into $L1_0$-MnAl instead of negative twin structure.

C. Discussion and outlook

Fundamentally speaking, as common crystal defects, both twin structure and dislocations can a bring dual effect on coercivity in the single-phase permanent magnets, the reduction of nucleation field, and the pinning effect. Recently, Zhao *et al.* [52–54] proposed a self-pinning mechanism, explaining the effect on the nucleation and pinning uniformly. This theory indicates that crystal defect in a magnet affects the process of nucleation and pinning simultaneously. The reduction of the local magnetic anisotropic field will generate the nucleation center of reversal domains on the location of defects, while the reversal domains will also be pinned at the defects owing to the gradient of magnetic parameters. When the external magnetic field becomes higher than the pinning field, the reversal domains propagate through the magnet. For twin structure, previous calculation and our experimental results suggest that the twins promote the nucleation process and do not enhance the pinning field, thus degrading the coercivity. This is because the symmetrical structure of twins locally lowers the anisotropy field, which is beneficial to the nucleation of reversal domains. While there is no severe lattice distortion or segregation, which weakens the difference between the magnetic parameters of twin structure and the perfect crystal lattice, the pinning effect is negligible. In contrast, dislocations show a strong pinning effect which enhances the coercivity. High density of dislocations will drastically decrease the nucleation field, but at the same time the severe lattice distortion is responsible for the pinning of the domain walls. The reversal domains will not move until the magnetic field is larger than the pinning field, which induces the huge coercivity in a HPT deformed magnet.

The comparison in magnetic performance (coercivity and saturated magnetization) between previous works and our study is illustrated in Fig. 12. The magnetic properties of $L1_0$-MnAl magnets obtained by different preparation methods, including ball milling and annealing, deforming, spark plasma sintering (SPS), melt spinning, as-cast, and annealing [28,31–34,55–60], are summarized in this figure. Besides, the twin-free $L1_0$-MnAl magnet investigated in this work as well as the HPT and annealed $L1_0$-MnAl magnets are also displayed on the graph. It is readily comprehensible that the magnetic properties in the upper right region of the graph are always superior to those in the lower left, based on which the graph is divided into region I and region II. The upper left of region I is filled by ball-milled powders, corresponding to a high density of lattice defects with quite high H_C, and severe lattice distortion leads to low M_s. The lower right part of region I is filled by melt-spun ribbons and as-annealed bulks, which generally present low density of defects to improve M_s, but with plenty of twin structure to weaken H_C. The center of region I is the as-annealed powders, as-deformed, and SPS bulks, corresponding to more complicated and mixed microstructure characteristics.

This work focuses on the regulating of microstructure by controlling the dislocation density as well as the presence

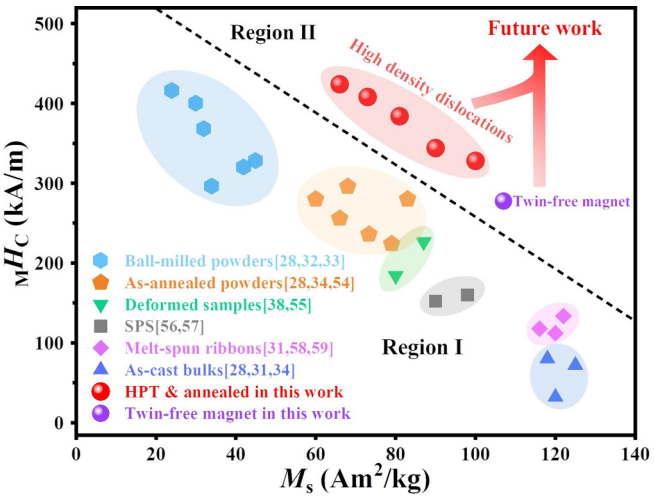

FIG. 12. The comparison of saturated magnetization and coercivity between $L1_0$-MnAl magnets obtained by a common preparation method ([28,31–34,55–60] and this work).

of twin structure, and this idea is proved to be beneficial to optimize the comprehensive magnetic properties. Obviously, our HPT and annealed MnAl magnets and the twin-free magnets located at the right upper part of this figure correspond to a better comprehensive magnetic performance. The combination of these two methods should be the key emphasis in future investigation of MnAl and other $L1_0$ rare-earth-free permanent magnets.

Based on the results above, the future development of the $L1_0$ permanent magnets requires the following two microstructural features:

(1) Absence of the twin structures.

(2) Nanograins with quite high density of dislocations.

However, most of the current fabrication methods cannot realize the ideal microstructure. Zhang *et al.* [29] have successfully obtained single-variant $L1_0$-MnAl without twin structure through thermal-mechanical coupling field performed on high-temperature $A3$ phase single crystal, presenting strong magnetic anisotropy. The earlier hot-extrusion MnAl magnets which undergo the treatment of thermal field and stress field simultaneously also show significantly better texture than the other kind of MnAl magnets [46,61,62]. Therefore, using the thermal-mechanical coupled field to treat the alloy with the high-temperature $A3$ phase is a possible pathway to eliminate the twins in order to enhance the coercivity and remanence simultaneously. The severe deformation, such as high-pressure torsion and equal channel angular pressing, has been proved to be able to form nanograins and introduce high density of dislocations. Therefore, the high-temperature severe deformation could be a promising method to realize the two microstructural features simultaneously. This method is considered to be the future fabrication method of $L1_0$ rare-earth-free permanent magnets, which may be able to promote their applications.

Both the above-discussed twin and dislocation structures are extensively observed defects in various types of materials. Actually, multiple types of microstructural defects have been adopted as a tool to optimize the mechanical properties

in structural materials [63–66]. Twin structures enhance the ductility drastically by stress induced twinning or twin boundary motion [63,64]; introducing dislocations can realize the "dislocation-strengthening effect" [65,66]. Recently, tailoring the physical properties via regulating the defects has also become a research focus in functional materials [67–72]. In ferroelectric materials, the pinning effect induced by dislocations leads to the formation of ferroelectric dead layers at interfaces, hence reducing the performance of ferroelectric devices [67,68]. Twinning in ferroelectric materials can increase the number of domain variants; the coercive field is reduced because the twin boundaries offers more domain nucleation sites to make the switching process easier [69]. In $MgSiO_3$ perovskite materials, the dislocation displays specific slip behaviors, resulting in good mechanical and plastic properties [70,71]. Antiphase boundaries (APBs) can promote the locally ordered $D0_3$ structures along them, which is considered to enhance magnetostriction [72]. In this context, tailoring defects are also, though less exploited so far, an important option to promote the development of the performance of functional materials.

IV. CONCLUSION

Our study of the correlation between the microstructure (with the focus on twins versus dislocations) and magnetic properties as well as the corresponding magnetic hardening mechanism in $L1_0$-MnAl permanent magnets can be summarized as follows:

1. Based on the comparison between the twin-free and twinned magnets, the twin structure is shown to degrade coercivity, remanence, and texture. The remanence and texture are deteriorated owing to the angle of $\sim 76°$ between the easy-magnetization axes along the twin boundary. The mechanism of coercivity is dominated by nucleation in as-annealed, melt-spun, directionally solidified, and some other general $L1_0$-MnAl magnets without the introduction of high density of dislocations, while twin boundaries tend to act as initial nucleation sites of the reversal magnetic domains. The coercivity of twinned magnets is decreased by approximately 50% in comparison with the twin-free magnets, which indicates that the twinned structure represents a negative effect.

2. The dislocations which are formed by HPT can act as a "strong" pinning center, thus modifying the dominant coercivity mechanism from nucleation to pinning. With the increasing annealing temperature, the morphologies of dislocation evolve from the nets to cells and finally to walls; the density of dislocation is also dramatically decreased. Consequently, the coercivity reduces from 424 to 328 kA/m while the pinning field remains unchanged, indicating the strong pinning effect on the domain wall motion. This means dislocations will affect the magnetic properties positively.

3. The outcome of this work indicates a pathway for the future development of the $L1_0$ rare-earth-free permanent magnets. The ideal microstructure should avoid the twin structures and contain nanograins with quite high density of dislocations. Therefore, the high-temperature severe deformation could be a promising method to realize these two microstructural features simultaneously. This original method may inspire alternative nano-/microstructure-engineering strategies for the development of $L1_0$ rare-earth-free permanent magnetic alloys which will allow the production of the desired structural features leading to high coercivities, bringing the materials closer to their physical limit.

ACKNOWLEDGMENTS

This work was supported by the National Natural Science Foundations of China (NSFC) under Grant No. 51520105002, the Beijing Natural Science Foundation (2202023), Fundamental Research Funds for the Central Universities, and China Scholarship Council. O.G. and K.P.S. thank the Deutsche Forschungsgemeinschaft (DFG, German Research Foundation), Project ID No. 405553726, TRR 270.

[1] J. M. D. Coey, New permanent magnets; manganese compounds, J. Phys.: Condens. Matter **26**, 064211 (2014).

[2] J. M. D. Coey, Permanent magnets: Plugging the gap, Scr. Mater. **67**, 524 (2012).

[3] O. Gutfleisch, M. A. Willard, E. Brück, C. H. Chen, S. G. Sankar, and J. P. Liu, Magnetic materials and devices for the 21st century: Stronger, lighter, and more energy efficient, Adv. Mater. **23**, 821 (2011).

[4] M. D. Kuz'min, K. P. Skokov, H. Jian, I. Radulov, and O. Gutfleisch, Towards high-performance permanent magnets without rare earths, J. Phys.: Condens. Matter **26**, 064205 (2014).

[5] J. Cui, M. Kramer, L. Zhou, F. Liu, A. Gabay, G. Hadjipanayis, B. Balasubramanian, and D. Sellmyer, Current progress and future challenges in rare-earth-free permanent magnets, Acta Mater. **158**, 118 (2018).

[6] J. M. D. Coey, Hard magnetic materials: A perspective, IEEE Trans. Magn. **47**, 4671 (2011).

[7] See Supplemental Material at http://link.aps.org/supplemental/10.1103/PhysRevMaterials.4.094402 for the theoretical magnetic properties of common L10 permanent magnets, the analysis of MAE of twin-free and twinned magnets, schematic diagram of high-pressure-torsion, and the MOKE images showing the nucleation type and pinning type during demagnetization process.

[8] T. Klemmer, D. Hoydick, H. Okumura, B. Zhang, and W. A. Soffa, Magnetic hardening and coercivity mechanisms in $L1_0$ ordered FePd ferromagnets, Scr. Metall. Mater. **33**, 1793 (1995).

[9] T. Burkert, L. Nordström, O. Eriksson, and O. Heinonen, Giant Magnetic Anisotropy in Tetragonal FeCo Alloys, Phys. Rev. Lett. **93**, 027203 (2004).

[10] J. H. Park, Y. K. Hong, S. Bae, J. J. Lee, J. Jalli, G. S. Abo, N. Neveu, S. G. Kim, C. J. Choi, and J. G. Lee, Saturation magnetization and crystalline anisotropy calculations for MnAl permanent magnet, J. Appl. Phys. **107**, 09A731 (2010).

[11] A. Edström, J. Chico, A. Jakobsson, A. Bergman, and J. Rusz, Electronic structure and magnetic properties of $L1_0$ binary alloys, Phys. Rev. B **90**, 014402 (2014).

[12] E. Poirier, F. E. Pinkerton, R. Kubic, R. K. Mishra, N. Bordeaux, A. Mubarok, L. H. Lewis, J. I. Goldstein, R. Skomski, and K. Barmak, Intrinsic magnetic properties of $L1_0$

FeNi obtained from meteorite NWA 6259, J. Appl. Phys. **117**, 17E318 (2015).

[13] M. Kotsugi, H. Maruyama, N. Ishimatsu, N. Kawamura, M. Suzuki, M. Mizumaki, K. Osaka, T. Matsumoto, T. Ohkochi, T. Ohtsuki, T. Kojima, M. Mizuguchi, K. Takanashin, and Y. Watanabe, Structural, magnetic and electronic state characterization of $L1_0$-type ordered FeNi alloy extracted from a natural meteorite, J. Phys.: Condens. Matter **26**, 064206 (2014).

[14] Z. Y. Jiao, Z. H. Fu, J. M. Wang, R. F. Zhang, and C. B. Jiang, Uniaxial magnetocrystalline anisotropy of tetragonal Mn_xGa_{100-x} ($50 \leqslant x \leqslant 75$) alloys, J. Magn. Magn. Mater. **489**, 165308 (2019).

[15] D. Odkhuu and S. C. Hong, First-Principles Prediction of Possible Rare-Earth Free Permanent Magnet of Tetragonal FeCo with Enhanced Magnetic Anisotropy and Energy Product Through Interstitial Nitrogen, Phys. Rev. Appl. **11**, 054085 (2019).

[16] K. P. Skokov and O. Gutfleisch, Heavy rare earth free, free rare earth and rare earth free magnets—vision and reality, Scripta Mater. **154**, 289 (2018).

[17] D. Palanisamy, D. Raabe, and B. Gault, On the compositional partitioning during phase transformation in a binary ferromagnetic MnAl alloy, Acta Mater. **174**, 227 (2019).

[18] Y. Tanaka, N. Kimura, K. Hono, K. Yasuda, and T. Sakurai, Microstructures and magnetic properties of Fe-Pt permanent magnets, J. Magn. Magn. Mater. **170**, 289 (1997).

[19] P. Müllner, B. E. Bürgler, H. Heinrich, A. S. Sologubenko, and G. Kostorz, Observation of the shear mode of the $\varepsilon \rightarrow \tau$ phase transformation in a Mn-Al-C single crystal, Philos. Mag. Lett. **82**, 71 (2002).

[20] T. Mix, K.-H. Müller, L. Schultz, and T. G. Woodcock, Formation and magnetic properties of the $L1_0$ phase in bulk, powder and hot compacted Mn-Ga alloys, J. Magn. Magn. Mater. **391**, 89 (2015).

[21] B. R. Bian, J. Du, W. X. Xia, J. Zhang, J. P. Liu, W. Li, Z. H. Guo, and A. R. Yan, Effect of reaction temperature on the shape of FePt nanoparticles, IEEE Trans. Magn. **50**, 2102704 (2014).

[22] N. I. Vlasova, G. S. Kandaurova, and N. N. Shchegoleva, Effect of the polytwinned microstructure parameters on magnetic domain structure and hysteresis properties of the CoPt-type alloys, J. Magn. Magn. Mater. **222**, 138 (2000).

[23] L. S. Wang, Z. H. Fan, and D. E. Laughlin, Trace analysis for magnetic domain images of $L1_0$ polytwinned structures, Scr. Mater. **47**, 781 (2002).

[24] J. P. Jakubovics, A. J. Lapworth, and T. W. Jolly, Electron microscope studies of ferromagnetic ordered structures, J. Appl. Phys. **49**, 2002 (1978).

[25] J. v. Landuyt, G. v. Tendeloo, J. J. v. d. Broek, H. Donkersloot, and H. Zijlstra, Defect structure and magnetic properties of MnAl permanent magnet materials, IEEE Trans. Magn. **14**, 679 (1978).

[26] S. Bance, F. Bittner, T. G. Woodcock, L. Schultz, and T. Schrefl, Role of twin and anti-phase defects in MnAl permanent magnets, Acta Mater. **131**, 48 (2017).

[27] S. Zhao, Y. Wu, Z. Y. Jiao, Y. X. Jia, Y. C. Xu, J. M. Wang, T. L. Zhang, and C. B. Jiang, Evolution of Intrinsic Magnetic Properties in $L1_0$ Mn-Al Alloys Doped with Substitutional Atoms and Correlated Mechanism: Experimental and Theoretical Studies, Phys. Rev. Appl. **11**, 064008 (2019).

[28] S. Zhao, Y. Y. Wu, C. Zhang, J. M. Wang, Z. H. Fu, R. F. Zhang, and C. B. Jiang, Stabilization of τ-phase in carbon-doped MnAl magnetic alloys, J. Alloys Compd. **755**, 257 (2018).

[29] C. Zhang, T. L. Zhang, J. M. Wang, S. Zhao, Y. Y. Wu, and C. B. Jiang, Anisotropic single-variant of $(Mn_{54}Al_{46})_{97}C_3$, Scr. Mater. **143**, 72 (2018).

[30] V. T. Nguyen, F. Calvayrac, A. Bajorek, and N. Randrianantoandro, Mechanical alloying and theoretical studies of MnAl(C) magnets, J. Magn. Magn. Mater. **462**, 96 (2018).

[31] Y. X. Jia, Y. Y. Wu, S. Zhao, J. M. Wang, and C. B. Jiang, Relation between solidification microstructure and coercivity in MnAl permanent-magnet alloys, Intermetallics **96**, 41 (2018).

[32] H. Jian, K. P. Skokov, and O. Gutfleisch, Microstructure and magnetic properties of Mn–Al–C alloy powders prepared by ball milling, J. Alloys Compd. **622**, 524 (2015).

[33] W. Lu, J. C. Niu, T. L. Wang, K. D. Xia, Z. Xiang, Y. M. Song, H. Zhang, S. Yoshimura, and H. Saito, Low-energy mechanically milled τ-phase MnAl alloys with high coercivity and magnetization, J. Alloys Compd. **675**, 163 (2016).

[34] Q. Zeng, I. Baker, J. B. Cui, and Z. C. Yan, Structural and magnetic properties of nanostructured Mn–Al–C magnetic materials, J. Magn. Magn. Mater. **308**, 214 (2007).

[35] H. L. Fang, S. Kontos, J. Ångström, J. Cedervall, P. Svedlindh, K. Gunnarsson, and M. Sahlberg, Directly obtained τ-phase MnAl, a high performance magnetic material for permanent magnets, J. Solid State Chem. **237**, 300 (2016).

[36] JCPDS—International Centre for Diffraction Data (2004), 12 Campus Boulevard, Newtown Square, PA 19073-3273, USA.

[37] M. Tyrman, S. Ahmim, A. Pasko, V. Etgens, F. Mazaleyrat, S. Quetel-Weben, L. Perrivère, and I. Guillot, Anisotropy of the ferromagnetic $L1_0$ phase in the Mn-Al-C alloys induced by high-pressure spark plasma sintering, AIP Adv. **8**, 056217 (2018).

[38] F. Bittner, J. Freudenberger, L. Schultz, and T. G. Woodcock, The impact of dislocations on coercivity in $L1_0$-MnAl, J. Alloys Compd. **704**, 528 (2017).

[39] P. Z. Si, H. D. Qian, C. J. Choi, J. Park, and H. L. Ge, A novel method for measuring the phase transformation temperature and enhanced coercivity in cold-rolled $MnAlC_x$ ($x = 0$) alloys, J. Magn. Magn. Mater. **451**, 540 (2018).

[40] J. G. Lee, X. L. Wang, Z. D. Zhang, and C. J. Choi, Effect of mechanical milling and heat treatment on the structure and magnetic properties of gas atomized Mn–Al alloy powders, Thin Solid Films **519**, 8312 (2011).

[41] P. Z. Si, J. Park, H. D. Qian, C. J. Choi, Y. S. Li, and H. L. Ge, Enhanced magnetic performance of bulk nanocrystalline MnAl-C prepared by high pressure compaction of gas atomized powders, Bull. Mater. Sci. **42**, 95 (2019).

[42] M. Yi, H. B. Zhang, O. Gutfleisch, and B. X. Xu, Multiscale Examination of Strain Effects in Nd-Fe-B Permanent Magnets, Phys. Rev. Appl. **8**, 014011 (2017).

[43] T. Schrefl, J. Fidler, and H. Kronmüller, Remanence and coercivity in isotropic nanocrystalline permanent magnets, Phys. Rev. B **49**, 6100 (1994).

[44] F. Maccari, L. Schäfer, I. Radulov, L. V. B. Diop, S. Ener, E. Bruder, K. Skokov, and O. Gutfleisch, Rapid solidification of $Nd_{1+x}XFe_{11}Ti$ compounds: Phase formation and magnetic properties, Acta Mater. **180**, 15 (2019).

[45] J. M. D. Coey, *Magnetism and Magnetic Materials* (Cambridge University Press, Cambridge, 2010).

[46] J. Thielsch, F. Bittner, and T.G. Woodcock, Magnetization reversal processes in hot-extruded τ-MnAl-C, J. Magn. Magn. Mater. **426**, 25 (2017).

[47] S. Zhao, Y. Y. Wu, J. M. Wang, Y. X. Jia, T. L. Zhang, T. L. Zhang, and C. B. Jiang, Realization of large coercivity in MnAl permanent-magnet alloys by introducing nanoprecipitates, J. Magn. Magn. Mater. **483**, 164 (2019).

[48] P. S. Prevéy, X-ray diffraction residual stress techniques, in *Metals Handbook*, Vol. 10 (American Society for Metals, Metals Park, OH, 1986), pp. 380–392.

[49] G. K. Williamson and W. H. Hall, X-ray line broadening from filed aluminum and wolfram, Acta Metall. **1**, 22 (1953).

[50] H. L. Buigs, A. Pomerleau, M. Fournier, and W. G. Tam, Implementation of a fast Fourier transform (FFT) for image processing applications, IEEE Trans. Acoust. **22**, 420 (1974).

[51] U. S. Ram, D. NG, and P. Gaunt, Magnetic viscosity and domain wall pinning in an MnAlC permanent magnet, J. Magn. Magn. Mater. **50**, 193 (1985).

[52] G. P. Zhao, X. L. Wang, C. Yang, L. H. Xie, and G. Zhou, Self-pinning: Dominant coercivity mechanism in exchange-coupled permanent/composite magnets, J. Appl. Phys. **101**, 09K102 (2007).

[53] G. P. Zhao, H. W. Zhang, Y. P. Feng, C. Yang, and C. W. Huang, Nucleation or pinning: Dominant coercivity mechanism in exchange-coupled permanent/composite magnets, Comput. Mater. Sci. **44**, 122 (2008).

[54] G. P. Zhao, L. Zhao, L. C. Shen, J. Zou, and L. Qiu, Coercivity mechanisms in nanostructured permanent magnets, Chin. Phys. B **28**, (2019) 077505.

[55] J. Rial, P. Švec, E.M. Palmero, J. Camarero, P. Švec, Sr., and A. Bollero, Severe tuning of permanent magnet properties in gas-atomized MnAl powder by controlled nanostructuring and phase transformation, Acta Mater. **157**, 42 (2018).

[56] Y. Kinemuchi, A. Fujita, and K. Ozaki, High-pressure synthesis of $L1_0$ MnAl with near-stoichiometric composition, Dalton Trans. **45**, 10936 (2016).

[57] A. Pasko, M. LoBue, E. Fazakas, L. K Varga, and F. Mazaleyrat, Spark plasma sintering of Mn-Al-C hard magnets, J. Phys.: Condens. Matter **26**, 064203 (2014).

[58] A. Pasko, F. Mazaleyrat, L. K. Varga, P. S. Stamenov, and J. M. D. Coey, High-field magnetization behavior of Mn-Al-C alloys, IEEE Trans. Magn. **50**, 2105104 (2014).

[59] P.Z. Si, H. D. Qian, X. Y. Wang, Y. Yang, J. Park, H. L. Ge, and C. J. Choi, High-pressure synthesis of high coercivity bulk MnAl-C magnets from melt-spun ribbons, J. Electron. Mater. **48**, 794 (2019).

[60] Z. Xiang, C. F. Xu, T. L. Wang, Y. M. Song, H. W. Yang, and W. Lu, Enhanced magnetization and energy product in isotropic nanocrystalline Mn55Al45 alloys with boron doping, Intermetallics **101**, 13 (2018).

[61] F. Bittner, L. Schultz, and T.G. Woodcock, Twin-like defects in $L1_0$ ordered τ-MnAl-C studied by EBSD, Acta Mater. **101**, 48 (2015).

[62] R. Madugundo, O. Koylu-Alkan, and G. C. Hadjipanayis, Bulk Mn-Al-C permanent magnets prepared by various techniques, AIP Adv. **6** 056009 (2016.

[63] S. Huang, H. Huang, W. Li, D. Kim, S. Lu, X. Li, E. Holmström, S. K. Kwon, and L. Vitos, Twinning in metastable high-entropy alloys, Nat. Commun. **9**, 2381 (2018).

[64] L. Lu, X. Chen, X. Huang, and K. Lu, Revealing the maximum strength in nanotwinned copper, Science **323**, 607 (2009).

[65] X. Li, Y. Wei, L. Lu, K. Lu, and H. Gao, Dislocation nucleation governed softening and maximum strength in nano-twinned metals, Nature **464**, 877 (2010).

[66] S. Jiang, H. Wang, Y. Wu, X. Liu, H. Chen, M. Yao, B. Gault, D. Ponge, D. Raabe, A. Hirata, M. Chen, Y. Wang, and Z. Lu, Ultrastrong steel via minimal lattice misfit and high-density nanoprecipitation, Nature **544**, 460 (2017).

[67] D. Liu, M. Chelf, and K. W. White, Indentation plasticity of barium titanate single crystals: Dislocation influence on ferroelectric domain walls, Acta Mater. **54**, 4525 (2006).

[68] A. Lubk, M. D. Rossell, J. Seidel, Y. H. Chu, R. Ramesh, M. J. Hÿtch, and E. Snoeck, Electromechanical coupling among edge dislocations, domain walls, and nanodomains in $BiFeO_3$ revealed by unit-cell-wise strain and polarization maps, Nano Lett. **13**, 1410 (2013).

[69] S. G. Cao, H. H. Wu, H. Ren, L. Q. Chen, J. Wang, J. Li, and T. Y. Zhang, A novel mechanism to reduce coercive field of ferroelectric materials via {111} twin engineering, Acta Mater. **97**, 404 (2015).

[70] P. Hirel, A. Kraych, P. Carrez, and P. Cordier, Atomic core structure and mobility of [100](010) and [010](100) dislocations in $MgSiO_3$ perovskite, Acta Mater. **79**117 (2014).

[71] P. Carrez, D. Ferré, and P. Cordier, Implications for plastic flow in the deep mantle from modelling dislocations in $MgSiO_3$ minerals, Nature **446**, 68 (2007).

[72] Y. C. Lin and C. F. Lin, Effects of phase transformation on the microstructures and magnetostriction of Fe-Ga and Fe-Ga-Zn ferromagnetic shape memory alloys, J. Appl. Phys. **117**, 17A920 (2015).